Role of ionization in imaging and spectroscopy utilizing fast electrons that have excited phonons

Juri Barthel [1,*] and Leslie J. Allen[2]

[1]*Ernst Ruska-Centre (ER-C-2), Forschungszentrum Jülich, 52425 Jülich, Germany*
[2]*School of Physics, University of Melbourne, Parkville, Victoria 3010, Australia*

Atomic resolution scanning transmission electron microscopy, based on counting fast electrons that have been scattered to large angles after exciting a phonon, so-called high-angle annular dark-field (HAADF) imaging, is widely used in materials science. Recently atomic resolution phonon spectroscopy has been demonstrated. In both cases experiments are usually modeled taking into account only elastic scattering and the inelastic scattering due to phonon excitation. However, other inelastic processes, such as plasmon excitation and single electron excitation, also play a role. In this paper we will focus on the role of ionization and its influence on imaging and spectroscopy based on phonon excitation. Inelastic scattering due to ionization is mainly forward peaked, which has implications for phonon spectroscopy with a detector in the forward direction. Nevertheless, a substantial fraction of electrons scattered by phonon excitation to larger angles have also lost significant amounts of energy due to also being involved in an ionization event. We discuss the implications of this for HAADF imaging and phonon spectroscopy utilizing electrons scattered to these larger angles.

I. INTRODUCTION

Scanning transmission electron microscopy (STEM) has developed into a versatile method for studying the structure of materials with spatial resolution at the atomic scale [1]. The high-angle annular dark-field (HAADF) mode of STEM has become the most widely used of the available modalities. This approach is based upon detecting electrons which have been scattered into an annular detector, usually with an inner angle around three times that of the probe-forming aperture and an outer angle substantially larger than the inner angle, as the probe is scanned across the specimen. This approach was placed on a quantitative footing in 2008 [2] and is capable of counting atoms or identifying the position of single dopant atoms when coupled with simulations [3,4]. The models used in making those simulations, such as the quantum excitation of phonons (QEP) model [5], consider only elastically scattered electrons and electrons which have excited phonons, which may entail excitation of multiple phonons in several such inelastic scattering events, the number of the latter depending on the thickness of the specimen.

In the HAADF imaging mode the electrons scattered into the angular range defined by the detector are simply counted and no analysis is made of the energy losses which, if only phonon excitation is considered, are expected to be small for electrons scattered into the detector, typically only tens or hundreds of meV. It is interesting to note that electrons scattered into the backward direction by repeated large angle scattering events can have cumulative energy losses of the order of 10 eV [6–8]. Recently improved monochromation of the source in STEM has made possible a resolution better

than 10 meV in electron energy-loss spectroscopy (EELS) [9–14] and allowed the phonon sector of the spectrum to be accessed for angles in the forward direction as well as for angles pertinent to HAADF imaging. It has been shown, using experiment in tandem with simulations in the QEP model, that changes in vibrational modes arising from defects such as interfaces, grain boundaries, and even individual atomic impurities can be probed with atomic resolution in STEM [15], particularly if one detects electrons that have been scattered out to angles approaching those used in HAADF imaging. This observation has been exploited to show that a single substitutional silicon impurity atom in free-standing graphene induces a characteristic, atomically localized modification of the vibrational response [16].

The use of the QEP model enables quantitative HAADF imaging and qualitative agreement with EELS maps (obtained by integrating over the phonon sector of the energy loss spectrum as a function of probe position). We emphasize again that the QEP model, as originally conceived [5], only takes into account elastic scattering and phonon excitation. Important conceptual differences between the QEP model and a frozen phonon model are discussed in Sec. III of Ref. [5]. The QEP model was recently extended to include the effects of plasmon scattering, which was shown to be important in getting the correct angular distribution for angles smaller than a typical HAADF inner angle [17]. Single electron excitations also make a contribution to the overall inelastic scattering; in particular, cross sections for less tightly bound electrons can be significant. Eaglesham and Berger [18] have discussed the amount of inelastic electron-electron scattering due to ionization into large angles by separating it from contributions due to phonon scattering. The latter is also often termed "thermal diffuse scattering." They find ratios of ionization scattering versus phonon scattering to be around one for light

*Corresponding author: ju.barthel@fz-juelich.de

elements and much smaller than one for heavier elements. Similar observations were made in another experimental study by Boothroyd *et al.* [19]. These experimental observations are related to what is referred to as electron Compton scattering—an EELS measurement where the collection aperture is placed at some angle relative to the incident beam, thus providing a cut through the Bethe surface [20]. Compton scattering can be interpreted as inelastic scattering of electrons from electrons in the target, where the target electron receives a significant energy and momentum and is ejected from its bound state, i.e., an atom is ionized, and we use the terms "ionization scattering" and "Compton scattering" interchangeably.

Here we investigate the effects of ionization from all atomic subshells, usually neglected in calculations, on STEM imaging using HAADF detectors and EELS in the phonon sector. One concern of this study is the conservation of flux by simulations when a large fraction of the electron beam has been involved in ionization events. Another is that combinations of phonon excitation, plasmon excitation, and ionization may occur, especially when electrons pass through a thicker sample. For example, electrons that have been involved in inelastic scattering by weakly bound target electrons, which is biased towards small angles, may subsequently be scattered to larger angles due to another inelastic scattering event involving phonon excitation.

II. MODELING INELASTIC SCATTERING

A. Calculating the effects of ionization

The QEP model [5] can be extended to calculate inelastic scattering due to ionization as a function of probe position in STEM. The fraction of incident electrons which mediate an ionization event can be expressed as a weighted average of contributions from the many possible atomic configurations in the specimen available to an incident electron as follows [21]:

$$I(\mathbf{R}, t) = \frac{1}{A^2} \sum_{j=1}^{J} \int_0^t \int_A \int_A \phi_j^*(\mathbf{R}, \mathbf{r}_\perp, z)$$
$$\times W(\mathbf{r}_\perp, \mathbf{r}_\perp') \phi_j(\mathbf{R}, \mathbf{r}_\perp', z) \, d\mathbf{r}_\perp d\mathbf{r}_\perp' dz. \quad (1)$$

The probe position is denoted by $\mathbf{R}$, t is the thickness of the specimen (along the z axis), A is the area of the unit cell, j labels a particular configuration of the atoms, and J denotes the number of different configurations. The probe function associated with the configuration j at a depth z is given by $\phi_j(\mathbf{R}, \mathbf{r}_\perp, z)$, where $\mathbf{r}_\perp$ is in the plane perpendicular to the z direction. In general the effective potential $W(\mathbf{r}_\perp, \mathbf{r}_\perp')$ for inelastic scattering is nonlocal—it depends on the two coordinates $\mathbf{r}_\perp$ and $\mathbf{r}_\perp'$. The signal also depends on the probe function at both $\mathbf{r}_\perp$ and $\mathbf{r}_\perp'$. This means that the relative phase of the probe function at points $\mathbf{r}_\perp$ and $\mathbf{r}_\perp'$ is relevant.

The projected nonlocal potential $W(\mathbf{r}_\perp, \mathbf{r}_\perp')$ is of the form

$$W(\mathbf{r}_\perp, \mathbf{r}_\perp') = \frac{2\pi m}{h^2 t} \sum_\alpha \sum_{n \neq 0} k_n H_{\alpha,n0}^*(\mathbf{r}_\perp) H_{\alpha,n0}(\mathbf{r}_\perp')$$
$$\times \int e^{2\pi i \mathbf{K}_\perp' \cdot (\mathbf{r}_\perp - \mathbf{r}_\perp')} \delta(k_n - K') d\Omega_{K'} dK', \quad (2)$$

where m is the relativistically corrected electron mass and k_n is the wave number for the inelastically scattered electron. In three dimensions the transition potentials for ionization have the form

$$H_{\alpha,n0}(\mathbf{r}) = \frac{e^2}{4\pi \epsilon_0} \int u_{\alpha,f}^*(\mathbf{r}') \frac{1}{|\mathbf{r} - \mathbf{r}'|} u_{\alpha,i}(\mathbf{r}') d\mathbf{r}', \quad (3)$$

where $u_{\alpha,i}(\mathbf{r})$ and $u_{\alpha,f}(\mathbf{r})$ represent initial- and final-state wave functions for the ionized electron in atom α in three dimensions. The prefactor contains the magnitude of the charge on an electron, e, and the permittivity of free space, ϵ_0.

To keep the calculations tractable, the approximation is made that we are ionizing neutral, isolated atoms. Initial bound states are described as products of spherical harmonics, describing the angular part, and Hartree-Fock radial wave functions with relativistic corrections [22]. Continuum wave functions are used to describe the final states after ionization as in Ref. [23]. Electron binding energies resulting from these calculations are comparable, certainly of the same order of magnitude, as those obtained using more sophisticated calculations taking into account ionicity or band structure. The assumption is that the simpler model with neutral atoms will provide a good indication of the effects of ionization in imaging and spectroscopy utilizing fast electrons that have excited phonons. This expectation is based on the fact that it is the binding energy of an electron and not the details of how it is bound which is the key element in determining the likelihood of ionization occurring.

The projected transition potential matrix element, as it appears in Eq. (2), is then

$$H_{\alpha,n0}(\mathbf{r}_\perp) \equiv \int_0^t H_{\alpha,n0}(\mathbf{r}) e^{2\pi i(K - K')z} dz \quad (4)$$

and $|H_{\alpha,n0}(\mathbf{r}_\perp)|^2$ gives the probability for inelastic scattering from atom α from an initial state 0 to a final state n. The wave number of the incident electron is K (corrected for refraction). The integration over $d\Omega_{K'}$ in Eq. (2) effectively integrates over all scattered electrons with wave vector $\mathbf{K}' = (\mathbf{K}_\perp', K_z')$ into that solid angle, subject to the requirement that the magnitude of $\mathbf{K}'$ is constrained by conservation of energy to be on the energy shell defined by $K' = k_n$. In Eq. (4) it has been assumed that $K_z' \approx K'$ (a good approximation for scattering which is predominantly in the forward direction). If the range of integration over $d\Omega_{K'}$ is sufficiently large then the effective potential for inelastic scattering is approximately local and Eq. (1) reduces to

$$I(\mathbf{R}, t) \approx \frac{1}{A^2} \sum_{j=1}^{J} \int_0^t \int_A |\phi_j(\mathbf{R}, \mathbf{r}_\perp, z)|^2 V(\mathbf{r}_\perp) d\mathbf{r}_\perp dz, \quad (5)$$

where $V(\mathbf{r}_\perp)$ is now a local effective ionization potential for scattering into the large solid angle that can be explicitly written as

$$V(\mathbf{r}_\perp) = \frac{\pi m}{h^2 t} \sum_{n \neq 0} \frac{1}{k_n} \sum_\alpha |H_{\alpha,n0}(\mathbf{r}_\perp)|^2. \quad (6)$$

Equation (5) formulates the fraction of the incident electrons that undergo inelastic scattering due to ionization of one subshell of a target atom, *including* electrons that have

already been thermally scattered (as a consequence of the summation over J atomic configurations). The contributions from electrons which have only been scattered elastically and those which have also been involved in phonon excitation prior to ionization can be separated [21]. The potential in Eq. (5) is usually evaluated in momentum space (see, for example, Ref. [23]), and the fact that it is local means that a parametrization of these Fourier coefficients, in terms of so-called inelastic scattering factors, is relatively straightforward. We extended the tables of inelastic scattering factors extant for the MUSTEM software [24] to include all subshells for B, N, O, Ti, and Sr for two simulation case studies in this work.

In order to calculate the amount of inelastic scattering into an angular range between θ_1 and θ_2, two sets of inelastic scattering coefficients are calculated, one for the angular range $0 \to \theta_1$ and one for the range $0 \to \theta_2$. Results for the angular range $\theta_1 \to \theta_2$ are then obtained by taking the difference of two separate STEM EELS image simulations, applying each set of inelastic scattering coefficients. First, simulations were performed including phonon excitation and, second, also without explicitly including phonon contributions but using absorptive potentials to take into account the effect of phonon excitation on the elastic channel. This procedure allows us to separate the inelastic scattering due to ionization after phonon excitation from ionization by electrons in the elastic channel in a straightforward way (see Sec. IV of Ref. [5] for a discussion of this point). The STEM imaging and EELS simulations were carried out for a series of small steps in sample thickness and then renormalized to take into account the total fraction of the incident beam involved in inelastic scattering, not just that due to phonon excitation, as will be discussed in the next section.

Finally in this section, we mention that another theory built on top of the QEP model, which also allows simulation of phonon EELS, has been reported by Zeiger and Rusz [25] and the findings in this paper are likely to also be of relevance in that approach.

B. Conservation of flux

While the cross sections for inner-shell ionization are several orders of magnitude smaller than that for phonon excitation, the probability that an electron is involved in outer-shell ionization is several orders of magnitude larger than for inner-shell ionization and can lead to a significant reduction in the proportion of electrons which have undergone elastic and phonon scattering only. For the purpose of renormalization to conserve flux, a third set of simulations was performed with the angular limitation removed for the calculation of inelastic scattering coefficients for ionization; i.e., ionization scattering into the full solid angle was taken into account. Elemental maps from this third set of simulations were summed up over all subshells of the atoms in a material for estimating the total amount of inelastic scattering due to ionization as a function of probe position and thickness. An iterative *a posteriori* renormalization scheme was then applied as illustrated in Fig. 1. In the initial calculations, the sum of fractional intensity involved in elastic and phonon scattering is kept normalized to unity at each probe scan position. In other words, the probe functions $\phi_j(\mathbf{R}, \mathbf{r}_\perp, z)$ in Eq. (5) are
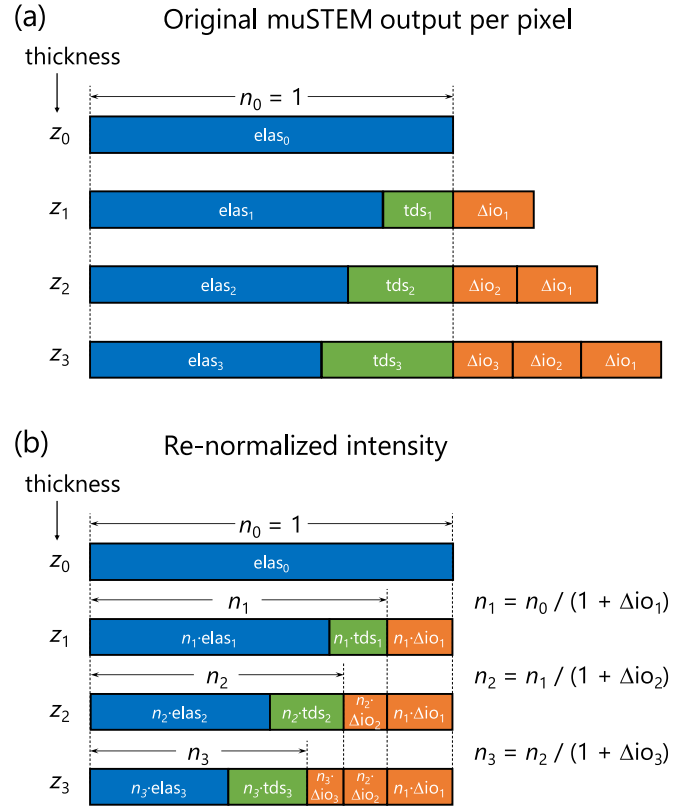

FIG. 1. (a) In the QEP simulations, for a given probe position, the elastic $elas_i$ (blue) and phonon excitation or thermal diffuse scattering components tds_i (green) are normalized to unity after each slice i with the tds component growing. At slice i the ionization contribution from that slice and previous slices has been accumulated, denoted $\Delta io_i, \Delta io_{i-1}, \dots, \Delta io_1$ (orange). (b) Iterative scheme for *a posteriori* renormalization of the calculation with initial normalization as in (a). Scaling factors n_i are applied iteratively to all components after each slice to preserve the electron flux.

not renormalized to take ionization into account. As indicated in Fig. 1(a), the additional images including ionization then lead to a total electron flux significantly greater than unity as the probe functions are propagated further along z into the specimen. In particular, when including ionization from all subshells, the additional intensity is significant. The STEM images calculated at steps z_i in specimen thickness related to elastic scattering ($elas_i$), thermal diffuse scattering (tds_i), and the change of intensity due to ionization (Δio_i) must therefore be scaled by factors

$$n_i = \frac{n_{i-1}}{1 + \Delta io_i}, \quad (7)$$

which depend on thickness and probe position, i.e., $n_i := n(\mathbf{R}, z_i)$. In what follows, the implicit dependence on probe position $\mathbf{R}$, as in Eq. (7), is omitted for reasons of clarity. The changes in total ionization scattering Δio_i are calculated by taking differences of EELS maps I_{io} obtained from thicknesses z_i and z_{i-1},

$$\Delta io_i = I_{io}(z_i) - I_{io}(z_{i-1}), \quad (8)$$

and by summation over the contributions from all atomic subshells.

Application of the renormalization procedure implies that the pertinent quantities should ideally be stored for each slice of a multislice calculation [26]. This can be a large amount of data, especially for thicker specimens. It suffices to renormalize after some larger steps in thickness, i.e., in steps of several slices in the QEP calculation. For the cases studied in this paper, this was done in steps of several unit cells, corresponding to steps in thickness of a few nanometers. Larger steps can be used without introducing a significant error when the changes Δio_i of total ionization scattering occurring with each step remain small. A check revealed that relative errors in normalization were less than 10^{-2} in the present study when compared to a unit cell sampling.

C. The relative roles of phonon excitation and ionization

We consider two possible pathways for an electron to be involved in both phonon excitation and ionization, in particular for those electrons measured at large scattering angles:

(1) Electrons may be first involved in phonon excitation and then mediate an ionization event.

(2) Electrons may be first involved in an ionization event and then undergo scattering due to phonon excitation.

Higher-order levels of such dual-type inelastic scattering involving both phonon excitation and ionization are neglected. For example, we do not consider that an electron can be involved in several ionization events. Considering that scattering due to phonon excitation is into larger angles than that due to ionization, we would expect this simplification to lead to a small underestimation of scattering to large angles and a concomitant small overestimation at small angles. There should be no further consequences of neglecting multiple ionization on conclusions in this paper as results are only discussed in discriminating general regions of the spectrum in EELS related to zero energy loss, energy loss due to phonon excitation, and the large range of energy losses beyond the phonon sector caused by ionization. This means that by undergoing one ionization event, a probe electron is assigned to the range of energy losses beyond the phonon sector and any further arguments only concern whether it is detected at small or large scattering angles.

While the first scenario is intrinsically how our calculations have been set up, the second scenario is less straightforward. Technically it would require propagating an electron through the material to the exit surface after an ionization event, taking into account further elastic and thermal diffuse scattering. There are also several final states possible in an ionization event and a large range of energies for the inelastically scattered electron, each of which would need to be considered separately, making such simulations prohibitively expensive for thick samples from a computational point of view. Therefore, an approximation was applied following arguments by Eaglesham and Berger [18] to estimate the intensity for the second scenario which would be expected for a detector at large scattering angles.

In this approximation, shown schematically in Fig. 2, we assume that the major contribution to scattering into large angles is due to the excitation of phonons and that ionization scattering is mainly forward peaked. Inelastic scattering due to ionization is calculated considering two angular ranges
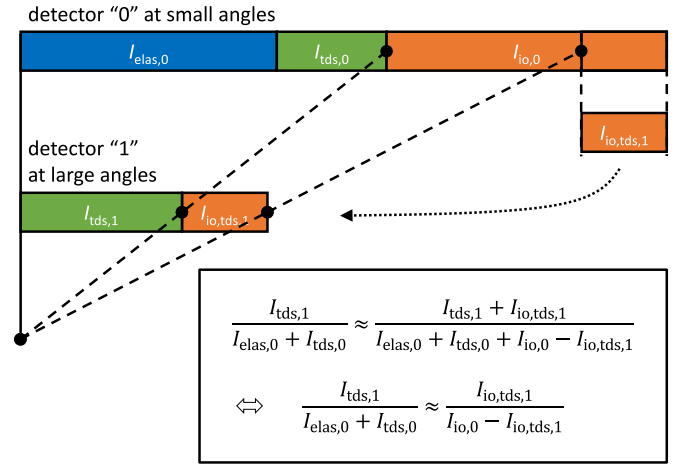

FIG. 2. Approximation of further phonon scattering after ionization ($I_{io,tds,1}$) effectively *shifting* intensity from a detector "0" at small scattering angles to a detector "1" at large scattering angles. This intensity is approximated by assuming an equal ratio of intensity between signal detected at large angles to that detected at small angles for fractions of the beam involved in elastic scattering (blue) and phonon scattering (green) only and for the remaining fraction, which is also involved in ionization (orange). The upper equation in the box describes equal horizontal length ratios in the drawing which represent intensity ratios. This is equivalent to the lower equation and Eq. (9). A vanishingly small elastic contribution at large scattering angles is assumed.

for EELS collection: (i) into small angles $0 \to \theta_1$ labeled by subscript "0" and (ii) into larger angles $\theta_1 \to \theta_2$ labeled by subscript "1" in what follows. Detection of elastic scattering and scattering due to phonon excitation is calculated for the same angular ranges. Taking the ratio of thermal diffuse scattering into large angles ($I_{tds,1}$) versus the sum of elastic and phonon scattering at small angles ($I_{elas,0} + I_{tds,0}$) as a template, a similar ratio is assumed between fractional intensities related to phonon scattering into large angles after ionization ($I_{io,tds,1}$) versus ionization scattering detected at small angles ($I_{io,0}$):

$$\frac{I_{tds,1}}{I_{elas,0} + I_{tds,0}} \approx \frac{I_{io,tds,1}}{I_{io,0} - I_{io,tds,1}}. \tag{9}$$

The difference in the denominator on the right-hand side of Eq. (9) takes into account that the intensity $I_{io,tds,1}$ is "removed" from small angles and added to large angles, thereby preserving the norm of the probe functions achieved by the previous renormalization of all components. An illustration of this approximation by assuming equal ratios and the *shifting* of intensity from small to large angles is illustrated in Fig. 2.

Solving Eq. (9) for $I_{io,tds,1}$ yields

$$I_{io,tds,1} \approx I_{io,0} \frac{I_{tds,1}}{I_{tds,1} + I_{ela,0} + I_{tds,0}}, \tag{10}$$

which is evaluated for EELS maps $I_{io,0}$ obtained after renormalization by the iterative procedure described above and separately for each specimen thickness and probe position. As already indicated for Eq. (9), EELS maps obtained for a detector at small angles must be reduced by $I_{io,tds,1}$, whereas those obtained for large scattering angles must be increased

accordingly. The smallest range of collection determined by θ_1 should be chosen large enough in order not to deviate too much from the local approximation made in Eq. (5). Also, to be consistent with Eq. (10), the angle θ_1 should be large enough to exclude a significant contribution of elastic scattering into the range $\theta_1 \to \theta_2$.

We note that we have implicitly made the assumption that the probe functions associated with electrons that have lost energy in an ionization event do not differ very much, at least in most cases, from the probe functions before ionization. This is a good approximation for scattering by target electrons in weakly bound and delocalized states, i.e., for scattering by electrons in the outermost subshells. A degree of similarity for probe wave functions before and after ionization has been noted also for ionization of "core-shell" electrons leading to a "preservation of elastic contrast" in simulations of elemental maps for energy-filtered transmission electron microscopy [27]. Furthermore, the approximation neglects that EELS maps have been accumulated from contributions of all atoms within the whole volume for a given specimen thickness. Consequently, further scattering for each of these incoherent contributions will follow slightly different dynamics and deviate from the ratio on the left-hand side of Eq. (9), which is evaluated only at one specimen thickness. Therefore, we expect an increasing error in the above approximation with increasing specimen thickness. The difference between calculations with and without ionization scattering deviates from the contribution due to ionization scattering alone and we attribute this deviation to an error in approximation. The error was found to be on the order of 0.1% fractional intensity below 1000 Å crystal thickness for both case studies presented in the following, and it has no effect on the conclusions drawn for phonon spectroscopy.

III. CASE STUDIES

Two case studies are presented, one for a material composed of light elements, boron nitride, and one with heavier elements, strontium titanate. The simulations were performed using MUSTEM, which is publicly available [24]. Additional software used to extend tables of inelastic scattering coefficients, to renormalize MUSTEM output including ionization, and to extrapolate phonon scattering towards large angles occurring after ionization is available on request from the corresponding author.

A. Boron nitride

The results reported by Eaglesham and Berger [18] suggest that the effects of ionization on electrons scattered into angles several times that spanned by the bright-field disk will be most important for light elements. Since hexagonal boron nitride (hBN) has also been used in several studies of phonon spectroscopy it is a good candidate for a case study. The only complicating factor is that hBN is polar and the model we employ here for ionization does not take that or other bonding effects into account. However, we have good estimates of binding energies and the issue of how the electrons are bound is less important for an estimation of the overall strength of ionization scattering.

In the simulations, the probe-forming aperture was 31.5 mrad and the hBN specimen was in a [0001] zone axis orientation relative to the incident probe of 60-keV electrons. Lattice constants of $a = 2.504$ Å and $c = 6.661$ Å for hBN in space group $P6_3/mmc$ were used, according to the model of Pease [28], with mean-squared amplitudes of thermal vibrations of 0.0121 Å^2 for B and 0.0092 Å^2 for N atoms [29]. Two structure slices were taken with thicknesses $c/2 = 3.331$ Å, ensuring that each slice contains one atomic layer of hBN. For the calculation of thermal diffuse scattering within the QEP model, 400 atomic configurations for each slice were generated assuming an Einstein model of uncorrelated atomic vibrations. Scattering factors, transmission functions, and propagators were sampled on grids of 384×384 points covering a rectangular supercell of 17.35 Å $\times$ 17.53 Å with the [$1\bar{1}00$] direction along the horizontal and the [$11\bar{2}0$] direction along the vertical grid axis. This sampling enables calculation of scattering up to angles of about 340 mrad. Neutral atoms are assumed and the scattering factors were taken from Waasmaier and Kirfel [30]. The lateral dimensions of the supercell may seem small for simulations using the convergent electron probe employed here and for the relatively large crystal thicknesses considered. Interference of overlapping probe tails due to the periodic boundary conditions assumed is likely. Therefore, we checked the effect of such interference artifacts on our results by performing simulations using a supercell of double the lateral dimensions. Deviations were found to be less than 1% in all the results shown, an insignificant effect.

The STEM image simulations were performed by scanning an aberration-free probe over a rectangular region of 4.337 Å $\times$ 2.504 Å, which corresponds to the projected area of two hBN primitive unit cells, using 12×7 scan steps, as determined by the Nyquist sampling rate [31]. In order to ensure convergence for the separation of elastic and inelastic scattering due to phonon excitations, an averaging over 100 Monte Carlo passes was applied per probe position, each with a different set of atomic configurations. Image series were calculated as a function of crystal thickness up to 1000 Å and in steps of 13.32 Å (two unit cells).

In Fig. 3 we show the average strength of ionization scattering of 60-keV electrons from hBN up to a scattering angle of 55 mrad. The mean intensity, in fractions of the incident beam current when scanning across the unit cell, is plotted as a function of crystal thickness. The contribution from the ionization of $1s$ electrons is small. However, ionization of L-shell electrons can become substantial even for thicknesses well below 200 Å. The strongest contribution here is found for the N $2p^3$ subshell, which is partly due to the lower binding energy common to all L-shell electrons (less tightly bound electrons are more easily ejected), but also due to the larger number of target electrons available for ionization in this particular subshell. Electrons which have only been involved in elastic scattering and ionization are the major component in the forward direction. The fraction of electrons which have undergone elastic scattering followed by excitation of phonons and then ionization is small for thicknesses less than 200 Å but is approaching the order of 10% for a specimen with a thickness of 1000 Å. At a thickness of more than 500 Å the majority of the beam electrons have already
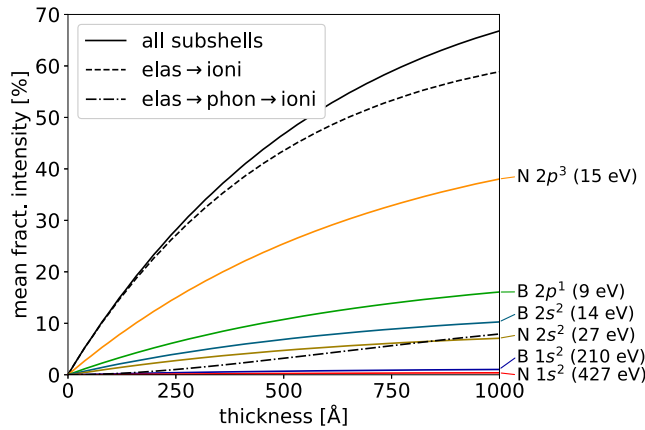
FIG. 3. Strength of inelastic scattering of 60-keV electrons from hBN due to ionization integrated up to 55 mrad scattering angle as a function of crystal thickness. The plotted intensity is an average obtained from simulations scanning the probe over one projected unit cell. Contributions from individual atomic subshells are displayed and the respective electron binding energies are those calculated using Hartree-Fock radial wave functions with relativistic corrections [22]. The intensities of ionization scattering from the elastic channel (elas → ioni) and that occurring after phonon scattering (elas → phon → ioni) are distinguished.
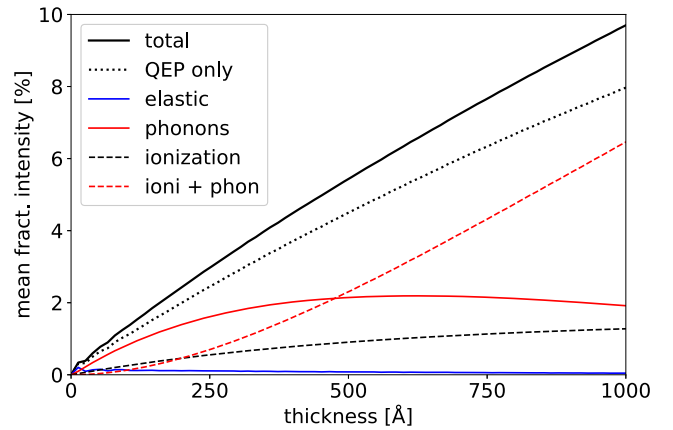

FIG. 4. Scattering of 60-keV electrons from hBN into the angular range of 55 to 99 mrad as a function of crystal thickness. The average intensity of STEM images is plotted from simulations including ionization (black solid) and simulations where ionization is ignored (black dotted). Different components of scattering contributing to the black solid curve are shown separately. A maximum of intensity for phonon spectroscopy (red solid) is expected around 500 Å crystal thickness.

been involved in an ionization event, showing that ionization involving outer-shell electrons is a strong effect. This has implications for phonon spectroscopy as further phonon scattering after an ionization event will not be registered in the low energy-loss range typical for phonon excitation. As the fraction of the beam involved in ionization increases with thickness, the remaining fraction due to elastic and phonon scattering decreases concomitantly. This in turn leads to a smaller increase in the fraction of the intensity involved in ionization, which is manifested in Fig. 3 as a decreasing slope with increasing thickness.

Figure 4 plots various components of the mean fractional intensity for the angular range from 55 to 99 mrad as a function of specimen thickness, separating elastic scattering, and inelastic scattering due to phonon excitation and ionization. This range of collection angles was chosen in accordance with the experiments on hBN presented by Hage *et al.* [15]. The black dotted curve in Fig. 4 also shows the total intensity as it would be obtained by a standard simulation within the QEP model, where ionization is neglected and renormalization has not been done. There is an obvious discrepancy between the two models for the total intensity expected at large scattering angles, which is mainly due to the additional inelastic scattering due to ionization. These curves indicate a large systematic error when neglecting ionization in HAADF STEM image simulations of low-Z materials.

The component due to elastic scattering is very small when compared to the total scattering of electrons into this angular range. This is in agreement with the assumptions made for our approximation of dual-type inelastic scattering to large angles. The fractional intensity due to inelastic scattering is broken down into three components. The component labeled "phonons" is that for electrons which have excited a phonon or multiple phonons in one or more such inelastic events. These

are the electrons that contribute to the phonon sector of the EELS spectrum and we expect a maximum in the spectrum for this component at a specimen thickness of about 500 Å. Electrons which are scattered to these large angles purely by ionization, i.e., by Compton scattering, are represented by the black dashed curve, and this component increases to about 1.3% of the incident probe current at a thickness of 1000 Å. It is at a significantly lower level than that for the same component expected in the forward direction (cf. black dashed curve in Fig. 3) in accordance with the general finding that angles are small for the majority of electron-electron scattering. The ratio of ionization scattering versus pure phonon scattering at these large angles is between 0.3 and 0.7, increasing with thickness. This ratio is of the same order of magnitude as that reported by Eaglesham and Berger for low-Z materials [18], despite differences in beam energy and detection geometry. Inner-shell ionization plays a stronger role among contributions from all shells here, compared to scattering in the forward direction. However, probe electrons that have been inelastically scattered by outer-shell electrons also dominate in ionization scattering to large angles. A significant contribution to large scattering angles by ionization involving the ejection of weakly bound electrons may seem implausible at first glance due to the small energy loss required as a minimum to allow this scattering process to happen. However, our calculations include all possible energy losses of the probe electrons, from the minimum given by the binding energy of the target electron up to the maximum set by the primary beam energy. This is taken into account by the sum over all possible final continuum states, labeled by n, in the effective local ionization potential of Eq. (6). The large energy losses included in this sum permit large momentum transfer and thus also electron-electron scattering to large angles. This is illustrated in Fig. 5 for the case of ionization scattering from the $2p$ subshell of a single oxygen atom, where the fractional intensity is plotted as a function of scattering angle and for
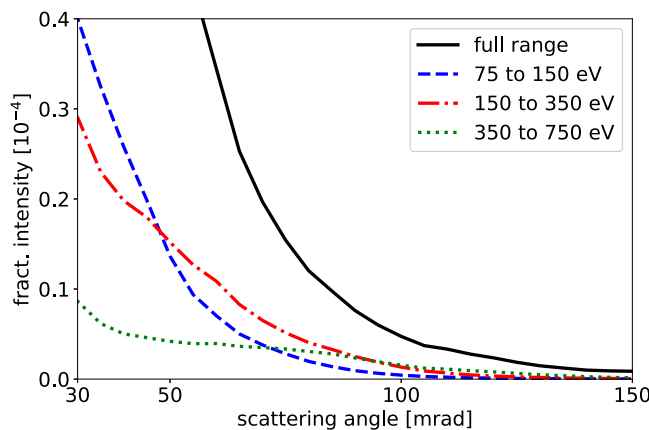
FIG. 5. Scattering of 60-keV electrons after ionization of the (four) electrons in the $2p$ subshell of a single oxygen atom, showing the intensity into a series of annular detectors, each covering a range of scattering angles and in steps of 5 mrad. Intensities, in fractions of the incident probe intensity, are plotted for three selected ranges of energy loss above the threshold energy for ionization, all showing notable contributions beyond 50 mrad. Also shown is the integral over all possible electron energy losses above the threshold energy.
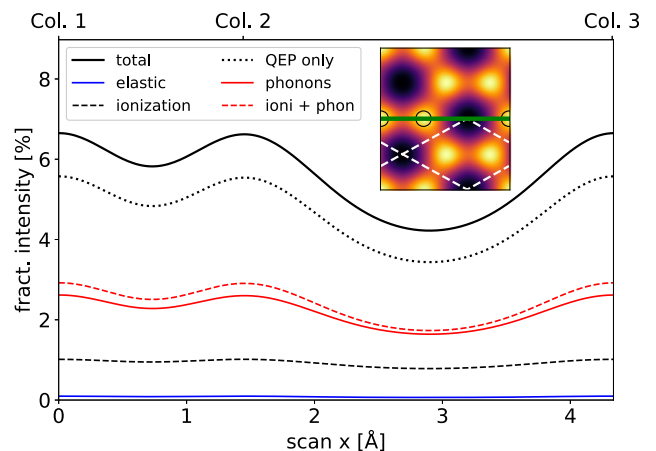

FIG. 6. Scattering of 60-keV electrons from hBN at 500 Å thickness into the angular range of 55 to 99 mrad as a function of probe position, corresponding to a HAADF scan line profile. Results of simulations including ionization (black solid) are shown in comparison to simulations where ionization is neglected (black dotted). Contributions to the black solid curve due to different scattering processes are separated. Maxima occur when the probe is placed over atomic columns. Inset is the scan image related to the black curve with the scan line marked by a green line, the [0001] hBN primitive unit cell indicated by white dashed lines, and positions of three atomic columns marked by circles.

several ranges of electron energy loss above the threshold energy. Scattering into the range beyond 50 mrad is dominated by energy losses of a few hundred eV and corresponds to fractional intensity of the order of 10^{-4}. Taking into account all atoms in a unit cell and all possible subshells sums to a fractional intensity of the order of 10^{-2} in the case of hBN illuminated by 60-keV electrons, as shown in Fig. 4.

In Fig. 4 the contribution "ioni + phon" contains electrons which have undergone both types of inelastic scattering along one of the two dual-type inelastic scattering paths considered in the calculations. This means they were involved in an ionization event and one or more phonon excitations before or after ionization. For a thickness larger than 500 Å, these electrons contribute the majority of inelastic scattering into large angles, and their contribution continues to increase approximately linearly with thickness. However, due to the larger energy losses occurring with ionization, these electrons would not be measured in the phonon sector of an energy-loss spectrum despite having been scattered to large angles by means of phonon excitation. Phonon excitation occurring with or without ionization is thus still the major mechanism causing scattering to large angles.

Ionization events have clear implications for the intensity that will be measured in the phonon sector of the energy-loss spectrum and there is an optimal thickness to maximize the signal. The renormalization factors applied to the phonon scattering contribution change very little as a function of probe position. Over the large range of sample thickness considered here, the variation of the renormalization factors as the probe is scanned across the specimen remained below 2%. Neglecting ionization in simulations of STEM EELS imaging using the phonon sector of an energy-loss spectrum as presented by Hage *et al.* [15] should therefore provide qualitatively correct images though fractional intensities are expected to be under-estimated by an approximately constant factor.

The fact that a large fraction of the electrons scattered into the HAADF region are no longer only involved in exciting phonons raises the question: "How well does quantitative HAADF work, especially on specimens containing lighter elements?" In order to study the influence of ionization scattering on HAADF imaging, we show a scan monitoring the HAADF signal across three atoms in Fig. 6 for a sample of 500 Å thickness and including the effect of partial spatial coherence due to an effective source size of 1 Å [full width at half maximum (FWHM)]. It can be seen that, at such a large thickness, the component due to pure phonon scattering and that also involved in ionization ("ioni + phon") are of approximately similar strength. It is due to the phonon scattering that both curves are similarly peaked at atomic columns.

The total intensity shown by the black solid curve in Fig. 6 is also compared to that of a calculation which includes only inelastic scattering due to phonon excitation but ignores ionization (black dotted curve) and has therefore also not been renormalized. The difference between these two models is essentially the direct inelastic scattering of electrons due to ionization (black dashed curve). This component shows only a weak dependence on probe position and effectively adds a constant background level. The HAADF detector is a bucket detector which does not discriminate in energy. The important issue is thus that most of the electrons are detected at large angles by such a detector because they have excited a phonon. Therefore, using a model considering only elastic scattering and phonon excitations is adequate up to some additional background and delocalization introduced by the electron-electron scattering. This means HAADF image simulations neglecting ionization still provide a good qualitative agreement but should not be used for quantitative analysis
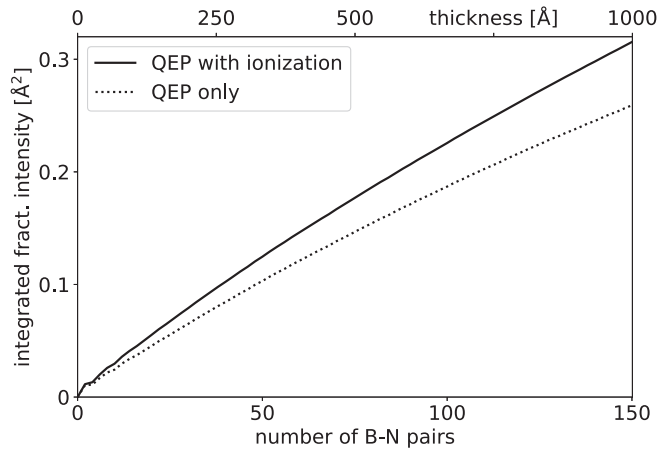
FIG. 7. Fractional intensity integrated over a circular area of 1 Å radius around atomic columns of [0001] hBN in simulated STEM images for a detector covering the angular range 55 to 99 mrad. The integrals obtained for a typical QEP calculation ignoring ionization (dotted) is compared to extended calculations including ionization and renormalization (solid) as a function of crystal thickness.

of images of thicker low-Z material samples. The difference found between simulations including ionization and those neglecting it has consequences in atom-counting approaches using simulations as a calibration reference [3]. A counting bias can be deduced from Fig. 7, which plots integrated fractional intensity extracted from HAADF STEM image simulations at positions of atomic columns as a function of crystal thickness. Along the [0001] direction of hBN, atomic columns are alternating sequences of boron and nitrogen atoms, and Fig. 7 therefore shows integrated intensity depending on the number of B-N pairs in a column. The integrals were calculated from total intensity maps containing phonon contributions only (dotted curve) and those also accounting for ionization and renormalization of the total intensity (solid curve). The integration is performed numerically according to

$$\tilde{I}_c = \frac{\Delta_u \, \Delta_v}{I_0} \sum_{\mathbf{R}_{u,v} \in A_c} I(\mathbf{R}_{u,v} - \mathbf{R}_c) \qquad (11)$$

by forming the sum over probe positions $\mathbf{R}_{u,v}$ of a STEM image $I(\mathbf{R})$ contained in a circular region A_c of radius 1 Å centered at an atomic column position $\mathbf{R}_c$. The integral $\tilde{I}_c$ is of square length unit after scaling by scan step sizes $\Delta_u = |\mathbf{R}_{u+1,v} - \mathbf{R}_{u,v}|$ and $\Delta_v = |\mathbf{R}_{u,v+1} - \mathbf{R}_{u,v}|$ along the horizontal and vertical direction of scanning (assuming equidistant steps for a rectangular scan field) and normalized by the incident probe current I_0. The column intensity integrals obtained from the two simulations already diverge for a very small number of B-N pairs, i.e., for a very thin crystal. As a consequence, quite large differences occur when using one or the other curve as reference for atom counting. Since hBN or other materials composed of only light elements are not typical candidates for quantitative HAADF imaging of thick samples, we will evaluate the implications of ionization on atom counting for the more representative case of SrTiO$_3$ imaged by 300-keV electrons in the next section.

B. Strontium titanate

A similar set of simulations for STEM imaging and EELS mapping was performed for SrTiO$_3$ viewed along the [001] zone axis. The targets of this case study are to investigate (i) the implications of ionization on quantitative STEM imaging, in particular for atom counting using HAADF STEM, and (ii) whether ionization scattering explains an overestimation of about 2% by simulations for intensity measured in the angular range below 64 mrad. Such an overestimation was found for simulations ignoring ionization scattering in comparison to experimental data for a SrTiO$_3$ crystal of about 200 Å thickness [17]. For consistency with this previous work, a 300-keV electron probe with a convergence semiangle of 23.5 mrad was used, an inner collection angle of $\theta_1 = 64$ mrad was chosen for the simulation of HAADF images, and an outer angle of $\theta_2 = 210$ mrad was assumed. Inelastic scattering by ionization of all 19 subshells (9 for Sr atoms, 7 for Ti atoms, and 3 for O atoms) was calculated with the same collection angles. For the purpose of renormalization, additional simulations were performed with inelastic scattering factors integrated over the full solid angle.

The simulations assume a structure model of cubic perovskite, SrTiO$_3$, according to Abramov *et al.* [32] with a lattice constant of 3.901 Å and thermal vibrations with mean-squared amplitudes of 0.0079 Å^2 for Sr, 0.0056 Å^2 for Ti, and 0.0093 Å^2 for O atoms. Structural slices were taken along the [001] direction at distances of 1.9525 Å, which separates alternating atomic planes of SrO and TiO$_2$. For each structure slice, 200 atomic configurations were generated assuming an Einstein model of uncorrelated atomic vibrations. Scattering factors, transmission functions, and propagators were sampled on a grid of 512×512 points covering a square region of 15.604 Å $\times$ 15.604 Å with the [100] direction along the horizontal and the [010] direction along the vertical grid axis. Due to this sampling, scattering angles up to about 215 mrad are included by the calculations. The aberration-free probe was scanned over one projected unit cell using 20×20 scan steps, consistent with the Nyquist sampling frequency [31]. By averaging over 100 Monte Carlo passes per scan point with different atomic configurations of the sample for each, convergence was ensured for the separation of elastic and inelastic scattering due to phonon excitation. The simulations were performed for a series over crystal thickness up to 1000 Å in steps of 31.21 Å (eight unit cells). For the evaluation of atom counting, an additional series limited to 250 Å thickness was calculated with steps of 3.901 Å in thickness corresponding to steps of one unit cell.

The average strength of inelastic scattering expected in the angular range 0–64 mrad is plotted in Fig. 8 as a function of crystal thickness. Compared to the hBN case, a lower fraction of the beam has been involved in ionization. For the thickness range below 500 Å, often used in high-resolution HAADF STEM imaging, this fraction remains below 25% of the incident probe current. The two strongest contributions by individual subshells of each atom type are shown and most of these strong contributions are related to ionization from subshells in which a larger number of electrons are in weakly bound states. Scattering by the O $2p^4$ electrons makes the largest contribution, which is mainly explained by
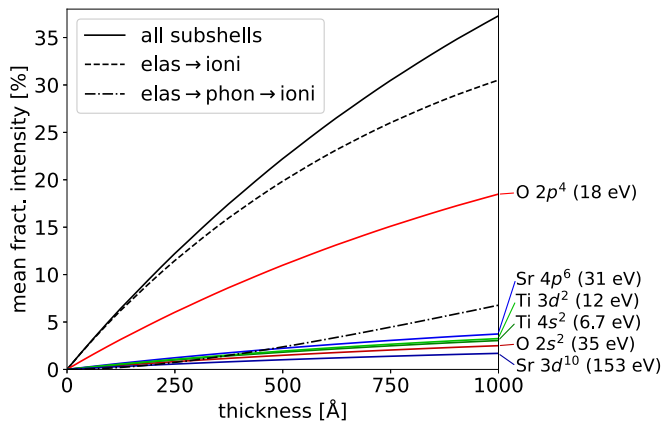
FIG. 8. Strength of inelastic scattering of 300-keV electrons from $SrTiO_3$ due to ionization up to 64 mrad scattering angle as a function of crystal thickness. The plotted intensity is an average obtained by scanning the probe over one projected unit cell. Contributions are shown for the two strongest subshells of each atom type with respective electron binding energies as calculated for Hartree-Fock radial wave functions with relativistic correction [22]. The intensity of ionization scattering from the elastic channel (elas → ioni) and that occurring after phonon scattering (elas → phon → ioni) are distinguished.

the three-times-higher density of oxygen atoms providing 12 target electrons per $SrTiO_3$ unit cell. In comparison, subshells with lower contributions to ionization have fewer electrons per unit cell, for example, six electrons for the Sr $4p^6$ subshell and two electrons for the Ti $3d^2$ subshell. Because of scaling by the number of target electrons, a subshell with slightly higher binding energy but more electrons can make a stronger contribution to ionization scattering than a subshell with lower binding energy but fewer electrons. Scattering of 300-keV electrons by $SrTiO_3$ expected beyond 64 mrad is plotted in Fig. 9 with different components separated. There is a very different contribution by the individual components compared
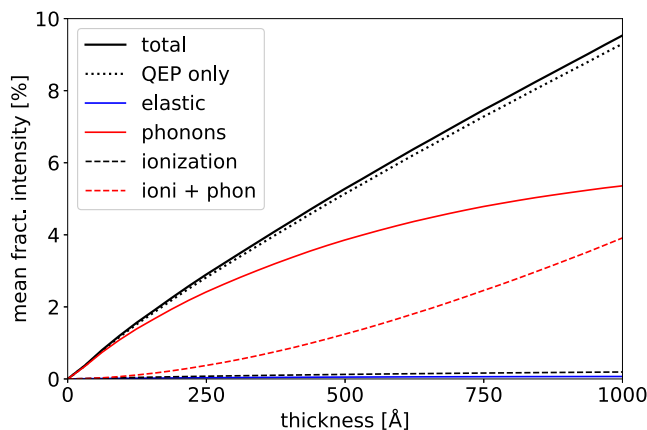

FIG. 9. Scattering of 300-keV electrons from $SrTiO_3$ into the angular range of 64 to 210 mrad as a function of crystal thickness. The average intensity of STEM images is plotted for simulations including ionization (black solid) and simulations where ionization is ignored (black dotted). Contributions to the black solid curve due to different scattering processes are separated.
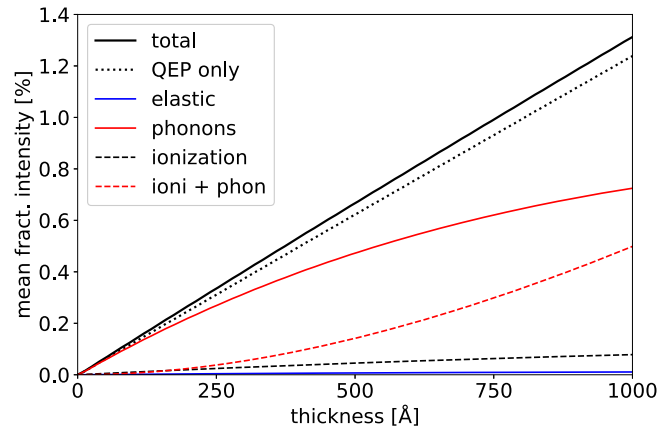

FIG. 10. Scattering of 300-keV electrons from hBN into the angular range of 64 to 210 mrad as a function of crystal thickness. The average intensity of STEM images is plotted for simulations including ionization (black solid) and simulations where ionization is ignored (black dotted). Contributions to the black solid curve due to different scattering processes are separated.

to the hBN case with 60-keV probe electrons, as shown in Fig. 4. Inelastic scattering due to phonon excitation (red solid curve) is stronger for $SrTiO_3$ and clearly the biggest contribution for the range of crystal thickness shown. Electrons which have been involved in ionization and phonon scattering (red dashed curve) become increasingly important for thicker samples. In simulations that included even larger thickness, not shown here, this component became the major contribution from about 1300 Å thickness on and a maximum of the pure phonon contribution was reached at about 1500 Å. Elastic scattering and Compton scattering are both very weak, with the latter remaining below 0.2% of the incident probe current up to a thickness of 1000 Å. Over this range of thicknesses, the ratio of Compton scattering versus phonon scattering is between 0.03 and 0.04. In agreement with the general trend found in experiments by Eaglesham and Berger [18], our simulations also suggest a much lower ratio for materials composed of heavier elements. Due to the very low level of Compton scattering in this case, the total mean fractional intensity obtained when including ionization (black solid curve) shows a smaller deviation from a calculation where ionization is neglected (black dotted curve). An immediate conclusion from this plot is that only small errors are expected when neglecting ionization in quantitative HAADF STEM imaging with higher beam energies and for a material containing heavier atoms. Second, the very low fraction of Compton scattering in this case also means that ionization scattering alone is not strong enough to explain the discrepancy between simulations and experiment observed by Barthel *et al.* [17], namely, the overestimation of simulations for intensity measured in the angular range up to 64 mrad. Further conclusions can be draw from Fig. 10, which plots the scattering of 300-keV electrons from hBN calculated under the same conditions applied in the $SrTiO_3$ case. In comparison to the simulations for hBN with 60-keV electrons in Fig. 4, there is a much smaller effect due to scattering involving ionization, as this contribution is an order of magnitude smaller at 300 keV. However, the amount of phonon scattering is also much lower. Comparison of Figs. 9
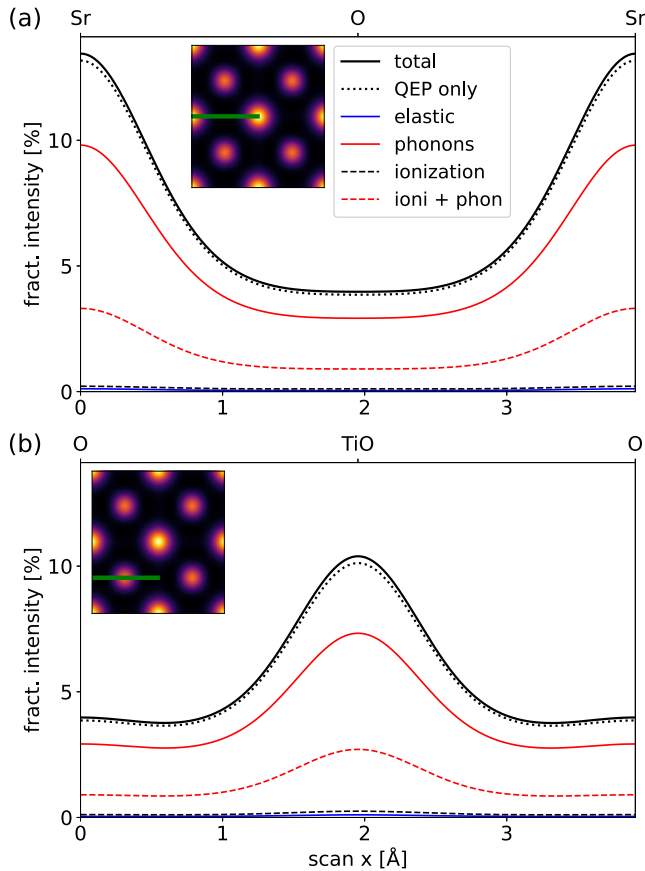
FIG. 11. Scattering of 300-keV electrons from SrTiO$_3$ at 500 Å thickness into the angular range of 64 to 210 mrad as a function of probe position. HAADF scan line profiles along the [100] direction are plotted (a) for a SrO plane and (b) for a TiO$_2$ plane. Results of simulations including ionization (black solid) are compared to simulations without ionization (black dotted). Contributions to the black solid curve due to different scattering processes are distinguished. The intensity is peaked at positions where the probe is placed over (a) Sr atomic columns and (b) Ti-O columns. Scan images related to the black solid curve are shown as insets for an area of 2 × 2 projected SrTiO$_3$ unit cells with the position of respective scan lines marked by green lines.

and 10, i.e., for the two materials imaged under otherwise identical conditions, shows that the relative effect of ionization scattering on images recorded at large scattering angles is stronger for a material consisting of only light elements. The ratio between ionization scattering and phonon scattering into the angular range 64–210 mrad is between 0.09 and 0.10 for hBN and thus larger than that found for SrTiO$_3$, namely, 0.03–0.04. The much better agreement between simulations applying the QEP model with and without ionization is also reflected in the line scan profiles displayed in Fig. 11. The line scans were extracted from simulated STEM images taking into account spatial incoherence due to a finite source size described by a Gaussian distribution of 0.8 Å width (FWHM). As expected for Z-contrast imaging, the highest-intensity peak is obtained when the probe is on atomic columns containing Sr ($Z = 38$) in Fig. 11(a), while a slightly lower peak occurs at Ti-O columns ($Z = 22 + 8$) in Fig. 11(b). No notable peak
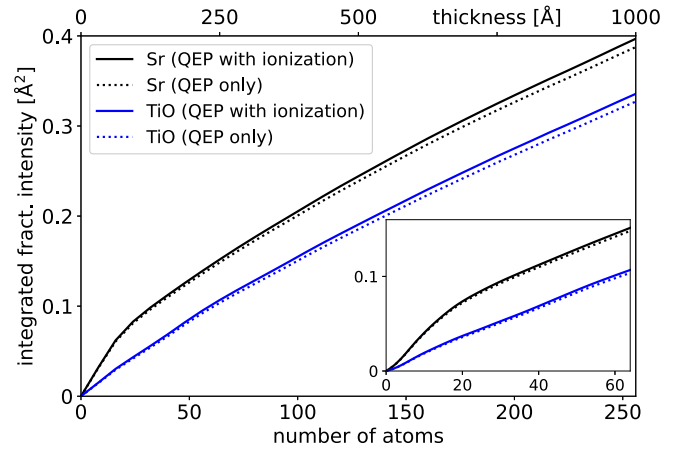

FIG. 12. Integrated fractional intensity from STEM images of [001] SrTiO$_3$ at atomic columns containing Sr (black) and Ti-O (blue). The dotted curves are calculated from QEP simulations neglecting ionization, while ionization and renormalization have been included for the solid curves. The plot includes columns of up to 256 Sr atoms or Ti-O atom pairs, corresponding to a crystal thickness of about 1000 Å. The inset shows a zoomed-in view of the range below 64 unit cells (250 Å thickness).

occurs when the probe is placed over pure oxygen atomic columns. There is also no peaked ionization scattering at the pure oxygen columns because of the large delocalization of the strong oxygen L-shell ionization.

Again a higher HAADF signal is expected when including ionization, although the difference is now much smaller compared to the case of hBN (cf. Fig. 6). Phonon scattering is clearly the major contribution at a crystal thickness of 500 Å but a significant fraction of scattered electrons has also been involved in ionization events, while elastic scattering is negligible. The contribution of electrons involved in ionization events is peaked at atomic columns, because the vast majority of these electrons are scattered to large angles by phonon excitations occurring after the ionization events. Integrals of fractional intensities in HAADF STEM images have been calculated according to Eq. (11) and are plotted in Fig. 12 as a function of thickness. The integrated intensity including ionization is only slightly larger compared to that of simulations neglecting ionization. Compared to the case of hBN, a much better agreement is found for the two models here, which means that only small errors are expected when applying the QEP model without corrections for the effect of ionization in quantitative analysis. This seems especially justified for thin crystals as shown by the inset of Fig. 12, where both models describe the same dynamics of large angle scattering and have only small differences for the two types of atomic columns. A small offset of integrated intensity as visible in Fig. 12 may still translate into a bias for atom counting considering that single atoms provide only small contributions to the integrated intensity of an atomic column. Different numbers of Sr atoms or Ti-O atom pairs would be deduced for the same value of integrated intensity from the two curves of each atom type. This difference in numbers of atoms, effectively the length of a horizontal line connecting the two curves at a given height, can be interpreted as a
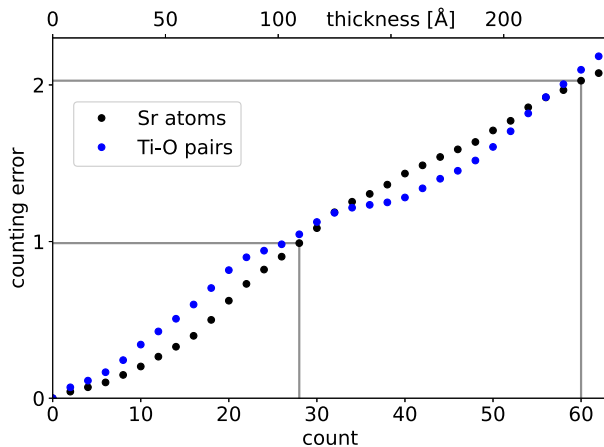
FIG. 13. Estimation of atom-counting errors on atomic columns of $SrTiO_3$ in [001] orientation made when neglecting the effect of ionization in simulations. The plot is limited to the regime below 250 Å crystal thickness. Error estimates are shown for counting Sr atoms and for Ti-O pairs based on the integrated intensities shown in Fig. 12. Horizontal and vertical lines mark the thicknesses at which a systematic counting error of one or two atoms, respectively, is expected.

counting error, assuming that the model which includes ionization effects predicts the integrated intensity for a given number of atoms (crystal thickness) more accurately. These differences have been plotted in Fig. 13. A positive counting discrepancy is obtained which means that neglecting ionization causes an overestimation of atom counts. The data are shown for crystal thicknesses below 250 Å, corresponding to 64 unit cells of $SrTiO_3$. A systematic error of approximately 3% is deduced for both types of column. For example, an overestimation of counting by one Sr atom and by one Ti-O pair is expected in respective columns with a length of 28 unit cells (110 Å). This increases to an error of two atoms at a thickness of 60 unit cells (234 Å).

IV. DISCUSSION

Inelastic electron-electron scattering has several implications for different modalities of STEM imaging as could be shown by including a model of such scattering in the two simulation studies presented above. It needs to be stated here though that this model can only provide an approximation for the overall strength of single electron-electron scattering as it is limited to scattering processes which leave the target electrons in unbound states; i.e., only ionization was included. The calculations include neither electronic excitation to bound states, such as interband or intraband transitions, nor collective excitation (plasmons). Inelastic scattering related to these other processes can be quite strong but is mostly into smaller angles due to the large delocalization of final states associated with the smaller energy losses compared to those occurring in ionization and the concomitant smaller momentum transfer for collective excitation [33,34]. Including these effects in calculations in addition to ionization would essentially further increase the fractional intensity of the probe involved in inelastic scattering to small angles with energy losses beyond

the phonon sector of a spectrum. Consequently, the fractional intensity available for phonon spectroscopy would be further decreased and a maximum of pure phonon scattering would occur at even smaller sample thickness. A modification of the conclusions regarding quantitative HAADF imaging and atom counting is not expected. While plasmon excitation can be a strong contribution in EELS of metallic and semiconductor materials [33], it should be of lesser concern for the two insulating materials discussed in this work. A previous study focusing on the effects of plasmon excitation on the angular distribution of scattering [17] did not show a significant influence on the large angular regimes in the case of strontium titanate.

Concerning inelastic scattering to small angles, our simulations show a very strong contribution due to ionization involving outer-shell electrons. Mean free paths for total ionization scattering calculated from the normalization factors applied in the two cases are about 700 Å and 1900 Å for hBN and 60-keV and 300-keV electrons, respectively, and about 1900 Å for $SrTiO_3$ and 300-keV electrons. These values agree at least to an order of magnitude with values in the literature (cf. Appendix C of Ref. [33]), indicating that our model provides reasonable estimates for the overall strength of inelastic electron-electron scattering. In total, ionization scattering is also stronger than phonon scattering as shown by the respective mean free paths listed in Table I. Our simulations are also consistent with a much smaller amount of ionization scattering to large angles. Although different materials and detection geometries were used, general agreement is found with the observations made by Eaglesham and Berger in that a higher ratio of electron-electron versus phonon scattering occurs at large angles for low-Z materials [18]. We also find that this ratio decreases for larger beam energies.

A sample thickness providing maximum intensity in the phonon sector of an electron energy-loss spectrum was deduced. This means that working with thicker samples to improve the signal-to-noise ratio for phonon spectroscopy has an upper limit. The limit found here could be checked in experiments with a setup similar to that used by Hage *et al.* [15] with hBN samples covering a range of thicknesses up to 1000 Å. The present results for hBN showed that a much lower fractional intensity is available for phonon spectroscopy compared to that deduced from traditional simulations. However, it was also found that this reduction of intensity in the phonon sector of an energy-loss spectrum depends only weakly on probe position. The qualitative appearance of images obtained by mapping the phonon sector in STEM EELS with high resolution should therefore not be strongly affected by ionization. The main reason for the weak dependence on probe position is the large delocalization of the strong inelastic scattering potentials for outer-shell ionization. Compared to these, the more localized potentials for inner-shell ionization have a relatively weak influence.

Ignoring the effects of ionization in HAADF STEM image simulations using the QEP model appears to be a good approximation for samples composed of heavier elements. From our simulations, a positive bias of only a few percent is manifested for atom counting with $SrTiO_3$ and 300-keV electrons. Assuming that an even lower bias can be expected for materials containing heavy elements such as gold, the

TABLE I. Kinematic mean free path (MFP) for ionization and phonon scattering, and the ratio of ionization to phonon scattering at large angles calculated for three cases.

Material	Beam energy (keV)	Kinematic MFP for ionization
hBN	60	700 Å
hBN	300	1900 Å
$SrTiO_3$	300	1900 Å
		Kinematic MFP for phonon excitation
hBN	60	4500 Å
hBN	300	13500 Å
$SrTiO_3$	300	2800 Å
		Ratio of ionization to phonon scattering into large angles
hBN	60	0.3–0.7
hBN	300	0.09–0.10
$SrTiO_3$	300	0.03–0.04

atom-counting results demonstrated by LeBeau *et al.* [3] should be accurate when the accompanying simulations take only elastic and phonon scattering into account. However, the present case study for hBN shows a substantial bias when neglecting ionization for materials composed of lighter elements and for imaging with lower beam energies. In such cases, the effects of ionization scattering can be of similar importance for quantitative STEM imaging as the need for calibrations of probe current, probe convergence, detector angles, and detector sensitivity as function of scattering angle [2,35,36], or the modeling of more complex sample properties such as static atomic displacements and amorphous layers [37–39].

V. CONCLUSION

In this paper we have explored the role of ionization in STEM imaging and spectroscopy based on simulations within the quantum excitation of phonons model. Compared to previous simulation studies, which considered mostly inelastic scattering with inner-shell electrons, contributions from all atomic subshells were taken into account here. Inelastic scattering due to ionization is a substantial contribution at lower beam energy and for materials composed of light elements. Most of the contribution is from outer-shell electrons, and it is mainly forward peaked. This has implications for the intensity of the signal in phonon spectroscopy with a detector in the forward direction. A substantial fraction of electrons scattered by phonon excitation to larger angles have also lost significant amounts of energy due to also being involved in an ionization event. For phonon spectroscopy utilizing electrons scattered to these larger angles, this leads to an optimal thickness where the maximum signal is expected. Scattering of an electron in the elastic channel by ionization to larger angles typically used for HAADF imaging is significant for light elements but less significant for heavy elements. Ratios between ionization and phonon scattering at large collection angles are consistent with the experimental data of Eaglesham and Berger [18]. This has implications for quantitative HAADF and counting of atoms in a column. For strontium titanate imaged with 300-keV electrons, systematic counting errors of up to two atoms for a thickness of 250 Å are possible if ionization is not taken into account, and a larger error is expected at lower beam energy and for materials composed of elements with lower atomic numbers.

ACKNOWLEDGMENTS

[1] S. J. Pennycook and P. D. Nellist, *Scanning Transmission Electron Microscopy: Imaging and Analysis* (Springer Science & Business Media, New York, 2011).

[2] J. M. LeBeau, S. D. Findlay, L. J. Allen, and S. Stemmer, Quantitative Atomic Resolution Scanning Transmission Electron Microscopy, Phys. Rev. Lett. **100**, 206101 (2008).

[3] J. M. LeBeau, S. D. Findlay, L. J. Allen, and S. Stemmer, Standardless atom counting in scanning transmission electron microscopy, Nano Lett. **10**, 4405 (2010).

[4] J. Hwang, J. Y. Zhang, A. J. D'Alfonso, L. J. Allen, and S. Stemmer, Three-Dimensional Imaging of Individual Dopant Atoms in $SrTiO_3$, Phys. Rev. Lett. **111**, 266101 (2013).

[5] B. D. Forbes, A. V. Martin, S. D. Findlay, A. J. D'Alfonso, and L. J. Allen, Quantum mechanical model for phonon excitation in electron diffraction and imaging using a Born-Oppenheimer approximation, Phys. Rev. B **82**, 104103 (2010).

[6] A. Winkelmann and M. Vos, Site-Specific Recoil Diffraction of Backscattered Electrons in Crystals, Phys. Rev. Lett. **106**, 085503 (2011).

[7] G. Argentero, C. Mangler, J. Kotakoski, F. R. Eder, and J. C. Meyer, Towards weighing individual atoms by high-angle scattering of electrons, Ultramicroscopy **151**, 23 (2015).

[8] B. D. Forbes and L. J. Allen, Modeling energy-loss spectra due to phonon excitation, Phys. Rev. B **94**, 014110 (2016).

[9] O. L. Krivanek, T. C. Lovejoy, N. Dellby, T. Aoki, R. W. Carpenter, P. Rez, E. Soignard, J. Zhu, P. E. Batson, M. J. Lagos, R. F. Egerton, and P. A. Crozier, Vibrational spectroscopy in the electron microscope, Nature (London) **514**, 209 (2014).

[10] T. Miyata, M. Fukuyama, A. Hibara, E. Okunishi, M. Mukai, and T. Mizoguchi, Measurement of vibrational spectrum of liquid using monochromated scanning transmission electron microscopy-electron energy loss spectroscopy, Microscopy **63**, 377 (2014).

[11] T. C. Lovejoy, G. C. Corbin, N. Dellby, M. V. Hoffman, and O. L. Krivanek, Advances in ultra-high energy resolution STEM-EELS, Microsc. Microanal. **24**, 446 (2018).

[12] K. Venkatraman, B. D. A. Levin, K. March, P. Rez, and P. A. Crozier, Vibrational spectroscopy at atomic resolution with electron impact scattering, Nat. Phys. **15**, 1237 (2019).

[13] O. L. Krivanek, N. Dellby, J. A. Hachtel, J.-C. Idrobo, M. Hotz, B. Plotkin-Swing, N. J. Bacon, A. L. Bleloch, G. J. Corbin, M. V. Hoffman *et al.*, Progress in ultrahigh energy resolution EELS, Ultramicroscopy **203**, 60 (2019).

[14] X. Yan, C. Liu, C. A. Gadre, L. Gu, T. Aoki, T. C. Lovejoy, N. Dellby, O. L. Krivanek, D. G. Schlom, R. Wu *et al.*, Single-defect phonons imaged by electron microscopy, Nature (London) **589**, 65 (2021).

[15] F. S. Hage, D. M. Kepaptsoglou, Q. M. Ramasse, and L. J. Allen, Phonon Spectroscopy at Atomic Resolution, Phys. Rev. Lett. **122**, 016103 (2019).

[16] F. S. Hage, G. Radtke, D. M. Kepaptsoglou, M. Lazzeri, and Q. M. Ramasse, Single-atom vibrational spectroscopy in the scanning transmission electron microscope, Science **367**, 1124 (2020).

[17] J. Barthel, M. Cattaneo, B. G. Mendis, S. D. Findlay, and L. J. Allen, Angular dependence of fast-electron scattering from materials, Phys. Rev. B **101**, 184109 (2020).

[18] D. J. Eaglesham and S. D. Berger, Energy filtering the "thermal diffuse" background in electron diffraction, Ultramicroscopy **53**, 319 (1994).

[19] C. B. Boothroyd, R. E. Dunin-Borkowski, and T. Walther, The scattering distribution from semiconductors as a function of angle and energy loss in the electron microscope, MRS Proc. **466**, 113 (1996).

[20] B. G. Williams, T. G. Sparrow, and R. F. Egerton, Electron Compton scattering from solids, Proc. R. Soc. London A **393**, 409 (1984).

[21] B. D. Forbes, A. J. D'Alfonso, R. E. A. Williams, R. Srinivasan, H. L. Fraser, D. W. McComb, B. Freitag, D. O. Klenov, and L. J. Allen, Contribution of thermally scattered electrons to atomic resolution elemental maps, Phys. Rev. B **86**, 024108 (2012).

[22] R. D. Cowan, *The Theory of Atomic Structure and Spectra* (University of California Press, Berkeley, 1981).

[23] M. P. Oxley and L. J. Allen, Atomic scattering factors for K-shell electron energy-loss spectroscopy, Acta Crystallogr., Sect. A: Found. Crystallogr. **57**, 713 (2001).

[24] L. J. Allen, A. J. D'Alfonso, and S. D. Findlay, Modelling the inelastic scattering of fast electrons, Ultramicroscopy **151**, 11 (2015).

[25] P. M. Zeiger and J. Rusz, Efficient and Versatile Model for Vibrational STEM-EELS, Phys. Rev. Lett. **124**, 025501 (2020).

[26] J. M. Cowley and A. F. Moodie, The scattering of electrons by atoms and crystals. I. A new theoretical approach, Acta Crystallogr. **10**, 609 (1957).

[27] H. G. Brown, A. J. D'Alfonso, B. D. Forbes, and L. J. Allen, Addressing preservation of elastic contrast in energy-filtered transmission electron microscopy, Ultramicroscopy **160**, 90 (2016).

[28] R. S. Pease, An X-ray study of boron nitride, Acta Crystallogr. **5**, 356 (1952).

[29] M. L. Odlyzko and K. A. Mkhoyan, Identifying hexagonal boron nitride monolayers by transmission electron microscopy, Microsc. Microanal. **18**, 558 (2012).

[30] D. Waasmaier and A. Kirfel, New analytical scattering-factor functions for free atoms and ions, Acta Crystallogr., Sect. A **51**, 416 (1995).

[31] C. Dwyer, Simulation of scanning transmission electron microscope images on desktop computers, Ultramicroscopy **110**, 195 (2010).

[32] Y. A. Abramov, V. G. Tsirelson, V. E. Zavodnik, S. A. Ivanov, and I. D. Brown, The chemical bond and atomic displacements in $SrTiO_3$ from x-ray diffraction analysis, Acta Crystallogr., Sect. B: Struct. Sci. **51**, 942 (1995).

[33] R. F. Egerton, *Electron Energy-Loss Spectroscopy in the Electron Microscope* (Springer Science & Business Media, New York, 2011).

[34] R. A. Ferrell, Characteristic energy loss of electrons passing through metal foils. II. Dispersion relation and short wavelength cutoff for plasma oscillations, Phys. Rev. **107**, 450 (1957).

[35] C. Dwyer, C. Maunders, C. L. Zheng, M. Weyland, P. C. Tiemeijer, and J. Etheridge, Sub-0.1 nm-resolution quantitative scanning transmission electron microscopy without adjustable parameters, Appl. Phys. Lett. **100**, 191915 (2012).

[36] S. D. Findlay and J. M. LeBeau, Detector non-uniformity in scanning transmission electron microscopy, Ultramicroscopy **124**, 52 (2013).

[37] V. Grillo, E. Carlino, and F. Glas, Influence of the static atomic displacement on atomic resolution Z-contrast imaging, Phys. Rev. B **77**, 054103 (2008).

[38] A. Rosenauer, T. Mehrtens, K. Müller, K. Gries, M. Schowalter, P. Venkata Satyam, S. Bley, C. Tessarek, D. Hommel, K. Sebald, M. Seyfried, J. Gutowski, A. Avramescu, K. Engl, and S. Lutgen, Composition mapping in InGaN by scanning transmission electron microscopy, Ultramicroscopy **111**, 1316 (2011).

[39] T. Grieb, M. Tewes, M. Schowalter, K. Müller-Caspary, F. F. Krause, T. Mehrtens, J.-M. Hartmann, and A. Rosenauer, Quantitative HAADF STEM of SiGe in presence of amorphous surface layers from FIB preparation, Ultramicroscopy **184**, 29 (2018).